Experimental determination of crystallization kinetic model of CENG-PCM composite material. Validation at macro and meso scales

Mariam Jadal, Jérôme Soto, Nicolas Boyard, Didier Delaunay

Applied Thermal Engineering

Experimental determination of crystallization kinetic model of CENG-PCM composite material. Validation at macro and meso scales

--Manuscript Draft--

Manuscript Number:	ATE-D-21-05371
Article Type:	Original Research Article
Keywords:	Latent heat storage; Phase Change Material; Expanded natural graphite; Crystallization kinetic
Corresponding Author:	Mariam JADAL, Dr. International University of Rabat: Universite Internationale de Rabat Rabat, FRANCE
First Author:	Mariam JADAL, Dr.
Order of Authors:	Mariam JADAL, Dr.
	Jérôme SOTO
	Nicolas BOYARD
	Didier DELAUNAY
Abstract:	This article presents a method for modelling the crystallisation kinetic of a phase change composite material when two transformations occur during the solidification. To obtain the full description of the crystallization process, the DSC analysis was completed with visualisations and extrapolations based on physical and analytical assumptions. This method has been validated successfully at different scales with paraffin and with paraffin embedded in Compressed Expanded Natural Graphite (CENG) matrix. The phase change material studied was a paraffin RT70HC from Rubitherm®. The validation experimental cases were performed on a plate of CENG-RT70HC composite cooled from its side and a packed-bed heat storage exchanger with a filler composed with encapsulated CENG-RT70HC capsules. The kinetic model was implemented in the finite element code Comsol® adding a source term to the energy equation. This model simulated closely the temperature evolution of a phase change material during a cooling. We found that the crystallisation kinetic is the same for the paraffin and for the paraffin with CENG showing that the CENG do not apparently affect the kinetic crystallisation of the paraffin.
Suggested Reviewers:	jean-pierre Bedecarrats jean-pierre.bedecarrats@univ-pau.fr
	Dominique Gobin dominique.gobin@centralesupelec.fr
	Laurent Zalewski laurent.zalewski@univ-artois.fr

Highlights:

- Two different crystallization mechanisms are observed in the PCM and are corroborated by a visualization experiment.
- Crystallisation kinetic modelling of a CENG-RT70HC composite is carried out by using Nakamura kinetics models for booth mechanisms.
- The crystallisation kinetic model is validated at micro and macro scales

Experimental determination of crystallization kinetic model of CENG-PCM composite material. Validation at macro and meso scales

Mariam JADAL[a,b,c], Jérôme SOTO[a,b], Nicolas BOYARD[a], Didier DELAUNAY[a]

[a] Université de Nantes, CNRS, Laboratoire de Thermique et d'Energie de Nantes, UMR 6607, La Chantrerie, rue Christian Pauc, BP 50609, 44306 Nantes Cedex 3, France
[b] Icam Ouest, 35 avenue du Champ de Manœuvres, 44470 Carquefou, France
[c] LERMA Lab, College of Engineering and Architecture, International University of Rabat, Parc Technopolis, Rocade de Rabat-Salé, Sala Al Jadida 11100, Morocco
* Corresponding author. Tel.: +33 2 40 68 31 57
E-mail address: mariam.jadal@univ-nantes.fr

ABSTRACT

This article presents a method for modelling the crystallisation kinetic of a phase change composite material when two transformations occur during the solidification. To obtain the full description of the crystallization process, the DSC analysis was completed with visualisations and extrapolations based on physical and analytical assumptions. This method has been validated successfully at different scales with paraffin and with paraffin embedded in Compressed Expanded Natural Graphite (CENG) matrix. The phase change material studied was a paraffin RT70HC from Rubitherm®. The validation experimental cases were performed on a plate of CENG-RT70HC composite cooled from its side and a packed-bed heat storage exchanger with a filler composed with encapsulated CENG-RT70HC capsules. The kinetic model was implemented in the finite element code Comsol® adding a source term to the energy equation. This model simulated closely the temperature evolution of a phase change material during a cooling. We found that the crystallisation kinetic is the same for the paraffin and for the paraffin with CENG showing that the CENG do not apparently affect the kinetic crystallisation of the paraffin.

Keywords

Latent heat storage
Phase change material
Expanded natural graphite
Crystallization kinetic

Nomenclature

C_p: thermal capacity, J k^{-1} kg^{-1}
h: partial enthalpy, J
ΔH: total enthalpy, J
m: mass, kg

n: Avrami exponent
K_{Avrami}: Avrami coefficient, s^{-n}
$K_{Nakamura}$: Nakamura coefficient, s^{-n}
T: temperature, °C
t: time, s
α: solidified fraction
ϕ: heat transfer rate, W
ρ: density, $kg.m^{-3}$

Abbreviations
CENG: Compressed Expanded Natural Graphite
DSC: Differential Scanning Calorimetry
ENG: Expanded Natural Graphite
PCM: Phase Change Material
TES: Thermal Energy Storage

1. Introduction

Phase Change Materials (PCM) are widely used for Thermal Energy Storage (TES) due to its capacity to store a high-density energy in narrow range of temperature variation. The applications are numerous in building [1–3], transport [4–7], electronic [8–10], solar power [11–13], domestic hot water [14,15] and industrial processes [16–18]. The thermal properties of the PCM are abundantly described in the scientific literature, using frequently a DSC analysis. The latent heat, the melting and freezing temperatures and the supercooling degree are reported in many publications. This description is performed, most of the time, using thermodynamic approach where the thermal capacity C_p or the enthalpy depend only on the temperature. However, sometimes, this description is not sufficient or incorrect when the PCM properties depend on temperature history. This situation is particularly true, when the PCM presents a supercooling property. In this case, a more complex model is necessary to describe the phase change, and many options are possible [19].

During the cooling phase, there are two types of approaches for studying the crystallization kinetics. The geometric approach, which formulates the volume occupied by semi-crystalline entities, and the probabilistic approach, which calculates the probability that an element of volume is transformed [20]. The main difference between these two approaches is the mathematical treatment, but the basic assumptions and the results are identical. In both cases, the phase change is modelized adding a source term that depends on time in the energy equation. When using the global approach, the kinetic behaviour of the PCM can be modelized using the Avrami model for isothermal transformation [21–23], Ozawa model for constant cooling rate transformation [24] or the Nakamura model for the generalised cases [25,26]. These characterisations are well known for polymers and paraffins. However, for PCM presenting a multiple step transformation, the references are less numerous. Hillier proposed a model for taking into account each transformation, that is commonly used today as T. Choupin [27] for a 40% PEEK and 60% carbon fibres composites, or by Gardner et al. [28] and Cortés et al. [29] for PEKK materials. We propose to apply this model to a PCM embedded in a thermal conductive matrix.

The conductive matrix is a Compressed Expanded Natural Graphite (CENG), used for enhancing the thermal conductivity of the PCM, around 0.2 $Wm^{-1}K^{-1}$ for a paraffin. This technique can improve the thermal conductivity magnitude up to two order depending on the CENG density [30] [31] [32] [33] [34]. The manufacturing process is described in the literature [35,36]. Some Latent Heat Thermal Energy Storage applications require this enhancement when the necessary heat transfer rate is high and the other heat transfer enhancing techniques such as fins or encapsulated PCM are not sufficient. For these applications, the phase change might occur very quickly, less than few minutes [33], and the kinetic behaviour of the PCM cannot be ignored.

The kinetic model of the crystallisation of a CENG-PCM occurring two phase transformation is original. We propose to discuss the method and the results for a composite CENG-PCM made of a RT70HC paraffin and a 2000 kgm^{-3} CENG. This composite has already been characterised including in an aging study [37] where is was shown that the crystallization of the RT70HC depends not only on the temperature, but also on the cooling rate. The purpose of this article is to determinate the crystallization kinetic model for each transformation of the CENG-PCM composite material, and, to validate the model at micro and meso scales. Therefore, the level of crystallinity and the morphology of the crystals formed during the cooling will be evaluated for each transformation. The phase change model will be established from the RT70HC characterisation and then applied for the CENG-RT70HC composite where the kinetic parameter might change due to nucleating agents.

2. Thermo-kinetic material characterization

2.1. Crystallisation kinetic observation using DSC

DSC tests were performed on a 3.6 mg sample of RT70HC at different heating and cooling rates, from 1 $K.min^{-1}$ to 30 $K.min^{-1}$, using a heat-flux, Thermal Analysis Q200 DSC device. The heating and cooling speeds are considered sufficiently low, and the sample sufficiently small to consider that the sample is isothermal. The sample was heated above its melting temperature at 90°C, then maintained at this temperature for five minutes to clear its thermal history, and finally cooled at 30°C. For all the tests, the latent heat, measured by integrating the heat flux curves, was the same for melting and solidification phases: 260 $kJ.kg^{-1}$. We can observe on the DSC test with 8 $K.min^{-1}$ presented in Figure 1 that the PCM presents a supercooling degree of 0.8 K and two exothermic peaks during the cooling phase. Two reasons could explain the presence of these two peaks: a solidification of two different populations in the sample or two transitions phase change mechanisms in a single component material, liquid-solid or solid- solid transformation.

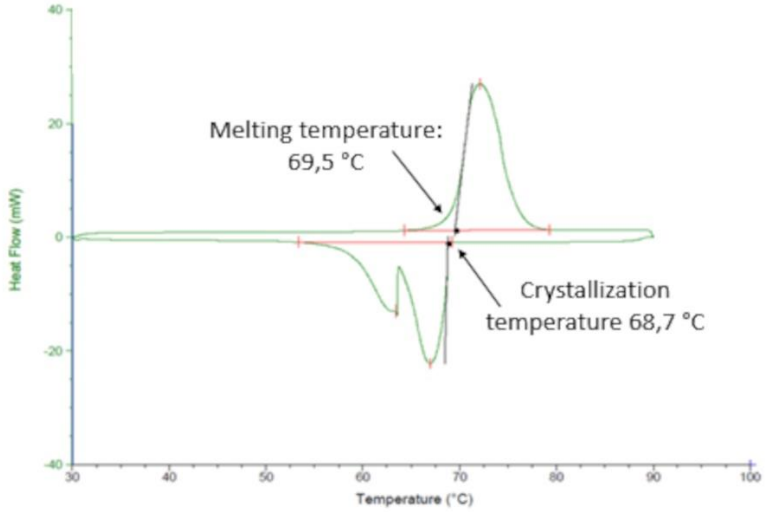

Figure 1: DSC for the RT70HC with 8K.min^{-1} cooling and heating rates

Figure 2 and Figure 3 showed respectively the DSC tests for different heating and cooling rates. We noticed that the onset melting temperature (Figure 2) remained unchanged by imposing different heating rates, while the starting solidification temperatures for each transformation (Figure 3) are affected by the cooling rate. It shows that the solid fraction depends not only on the temperature but also on the time.

We propose to separate the peaks to study separately the kinematic behaviour and to observe the sample during its solidification to identify the kinetic crystallization morphology (section II.2.b).

The DSC analyses of RT70HC and CENG-RT70HC composite for the same heating and cooling rates, 8K min^{-1}, are shown in Figure *4*. The portion RT70HC in CENG cannot be assessed accurately in the 3.6 milligram sample. Therefore, the heat flow magnitudes cannot be compared between the two samples unlike the onset phase change temperatures. We can notice that the CENG does not significantly affect these temperatures as the onset melting temperatures are 69.5°C for the RT70HC and 69.4°C for the composite. The onset crystallization temperatures are, for the first transformation 69.8°C for RT70HC and 69.7°C for the composite material and for the second transformation 63.8°C for RT70HC and 63.5°C for the composite material. We can also remark that CENG-RT70HC heat flow distribution for the second transformation of crystallization operates at lower temperatures compared to the RT70HC. This phenomenon required further investigation to understand this behaviour. These observations between the RT70HC and the CENG-RT70HC samples led us to assume that the kinetic behaviours of the two materials might be the same.

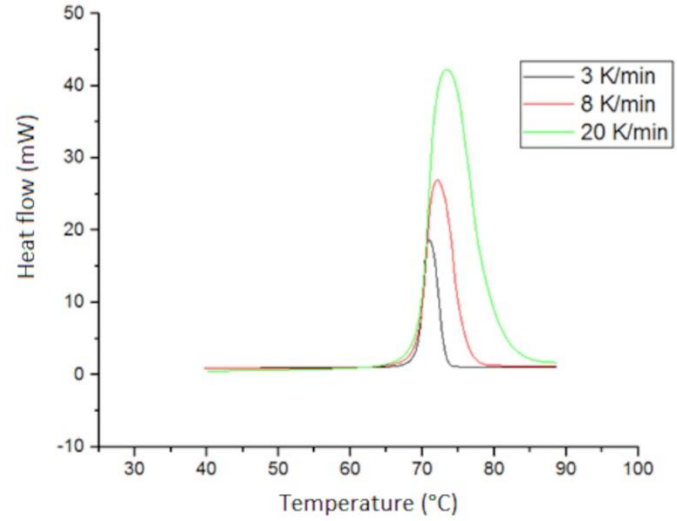

Figure 2: DSC analysis of RT70HC for different heating rates

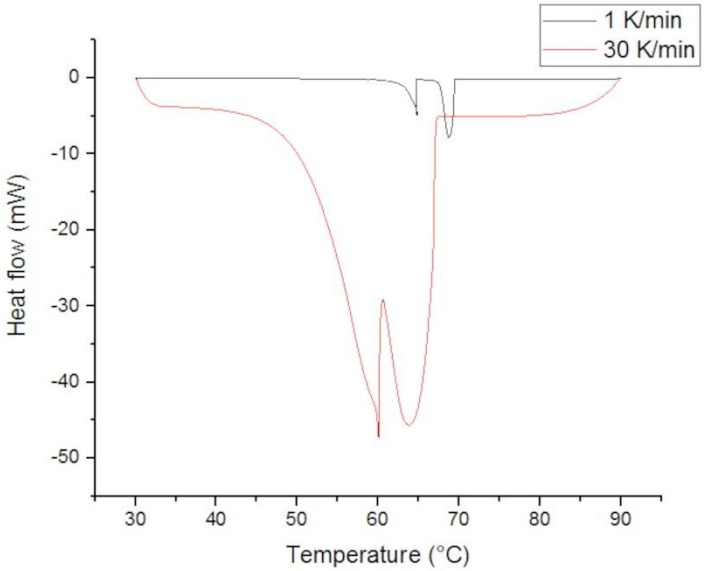

Figure 3: DSC analysis of RT70HC for different cooling rates

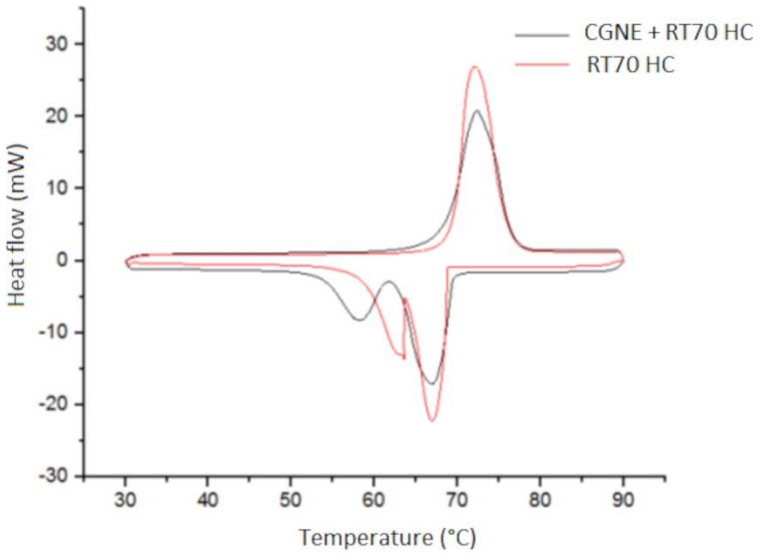

Figure 4: DSC analysis of RT70HC and CENG-RT70HC

2.2. Crystallisation kinetic model

2.2.1. Avrami isothermal kinetic model

Few models describe the crystallization kinetic. The Avrami model where the crystallization kinetic is observed in isothermal conditions gives the solidified fraction *α (t, T)* as shown by Equation 1.

$$\alpha(t,T) = 1 - exp(-K_{AV}(T).t^{n}) \qquad \text{Equation 1}$$

where K_{AV} is a coefficient that depends on the isothermal temperature *T*, *t* is the time of the transformation, and, the exponent *n* is determined by the crystallisation morphology and germination mechanism [21].

The solid fraction evolution *α(t, T)* was determined using the DSC device, where the PCM sample was cooled from 90°C, while the PCM is fully liquid, to a temperature in the range of the temperatures of the PCM crystallization. This process was performed for the two transformations (Figure 5).

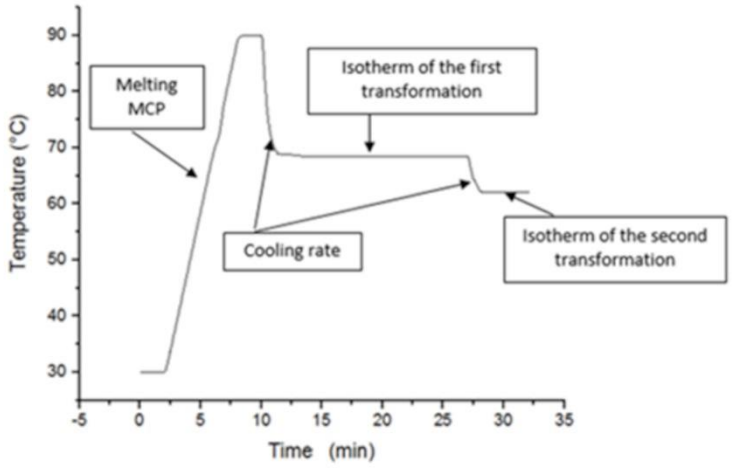

Figure 5: Thermal cycle imposed on PCM

The experiment was performed for ten end cooling temperatures. Each time, the heat flux was measured by the DSC and the partial energy of crystallization, *h(t)*, was determined by integrating the heat flux of the peak versus time for each transformation (Figure 6). The isothermal temperature was maintained at least for 20 minutes for the first transformation and 10 minutes for the second.

The isothermal crystallization measurements of RT70 HC was carried out between 67.5 and 69.3 °C for the first peak, and between 62.5 and 63.5°C for the second peak. Figure *7* and Figure *8* showed respectively an example of the isothermal results obtained for 68, 68.5, 69°C and 62.5, 63°C. It can be observed that as the isothermal temperature increases, the time at which the heat flow reaches its maximum is significantly shorter. We noticed also that the crystallization duration of the second transformation is shorter than the first transformation. Indeed, the first peak appears during a couple of minutes and a few seconds for the second peak.

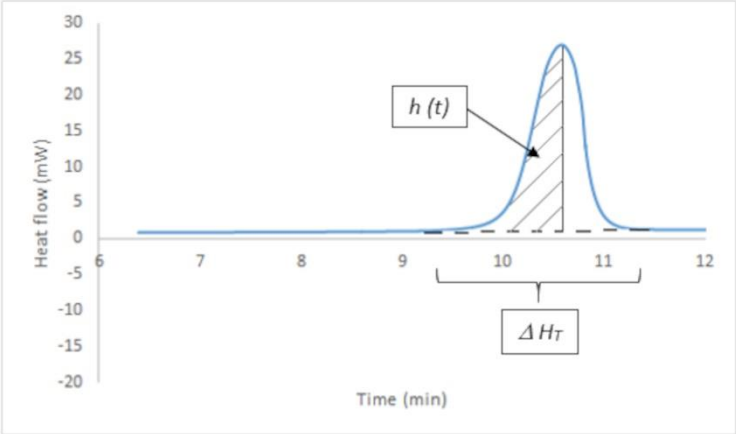

Figure 6: Methodology for calculating the solidified fraction $\alpha(t)$ using the partial enthalpy $h(t)$ and the total enthalpy ΔH_T

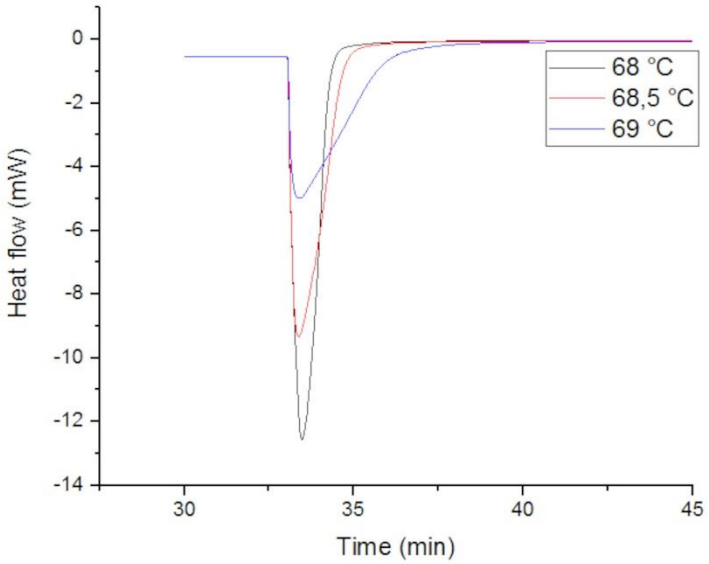

Figure 7: DSC analysis showing the heat flow for the first peak versus time during the isothermal crystallization of RT70HC at different temperatures

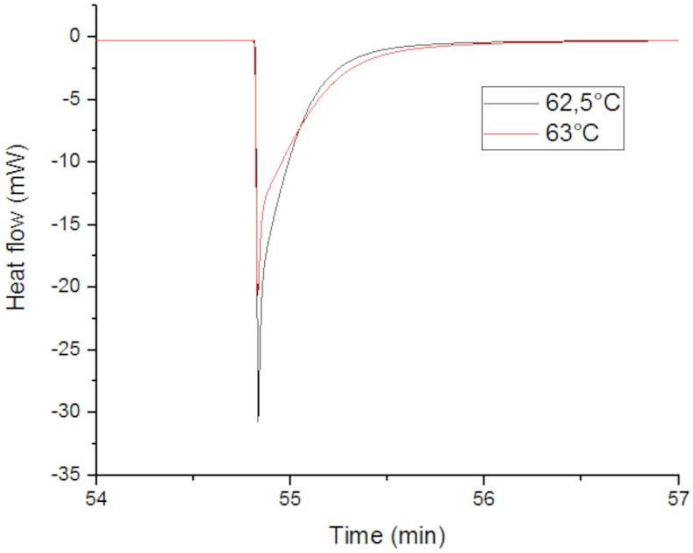

Figure 8: DSC analysis showing the heat flow for the second peak versus time during the isothermal crystallization of RT70HC at different temperatures

The ratio of the partial energy *h(t)* with the total latent heat of the transformation ΔH_T, gives the solidified fraction $\alpha(t)$ defined as the ratio of the mass of sample crystalized at a given time *t* and the mass of the final crystallizable PCM.

$$\alpha(t) = \frac{h\,(t)}{\Delta H_T} \qquad \text{Equation 2}$$

The Figure 9 and Figure 10, show typical results from DSC analysis for the first and second transformation. This method allows to separate each peak and to measure the partial latent heat

enthalpy for the first transformation ΔH_1 = 180 KJ.kg^{-1} and for the second transformation ΔH_2 = 74 KJ.kg^{-1}. The enthalpy sum of the two transformations, ΔH_T = 254 kJ.kg^{-1}, is close to that obtained previously without the two peaks separation in the anisothermal case. We estimate that this difference is small enough i.e. 2%. Therefore, the two transformations are considered correctly from the energy conservation point of view.

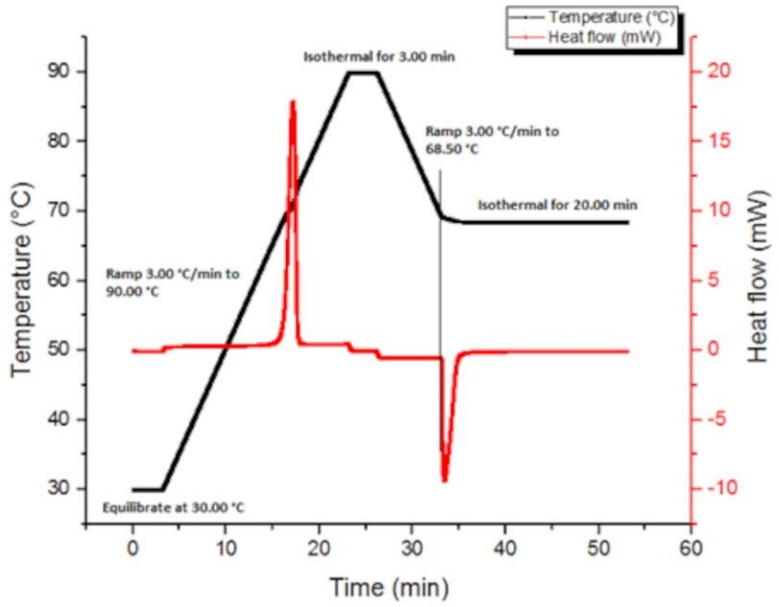

Figure 9: DSC Time evolution of heat flux and temperature for the first transformation

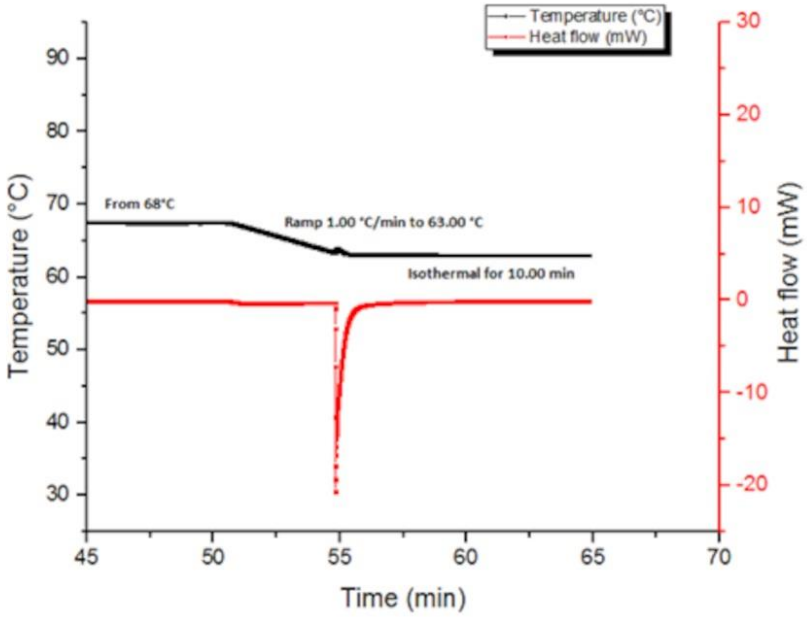

Figure 10: DSC time evolution of heat flux and temperature for the second transformation.

From the DSC results, the solidified fraction was calculated by Equation 2 and plotted for different temperature in Figure 11 for the first transformation and in Figure 12 for the second transformation. We denote α_1, the solidified fraction of the first transformation and α_2 for the second.

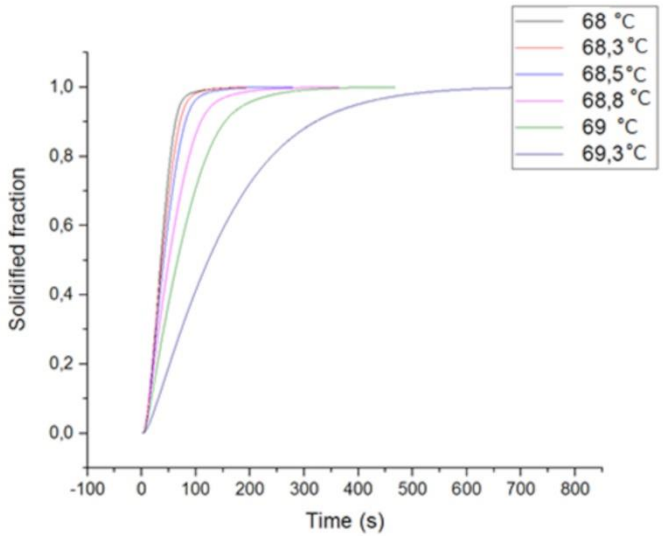

Figure 11: Time evolution of the partial solidified fraction α_1 for the first transformation

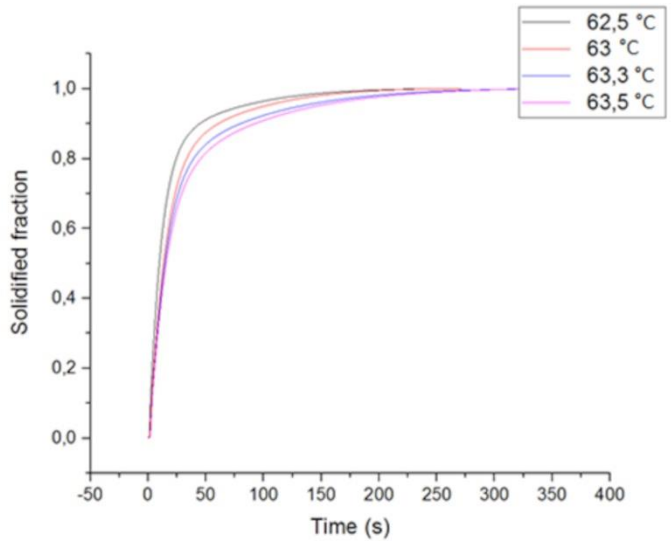

Figure 12: Time evolution of the partial solidified fraction α_1 for the second transformation

To identify the Avrami parameters model, the Equation 1 can be linearized as followed:

$$\ln[-ln(1-\alpha(t))] = \ln[K_{Avrami}(T)] + n.ln(t) \qquad \text{Equation 3}$$

Therefore, by plotting the function ln $(-ln\ (1-\alpha))$ versus ln (t), the slope of the straight line gives the exponent of Avrami n, and the coefficient K_{Avrami}, can be obtained from the ordinate of the y-axis intersection. The straight lines are taken in the linear parts of the curves i.e. when the values of α is between 0.08 and 0.9 for the first transformation (Figure 13) and from 0.4 to 0.9 for the second transformation (Figure 14). As shown in Table 1, the mean value of *n* for the first transformation is close to 2 and to 1 for the second transformation.

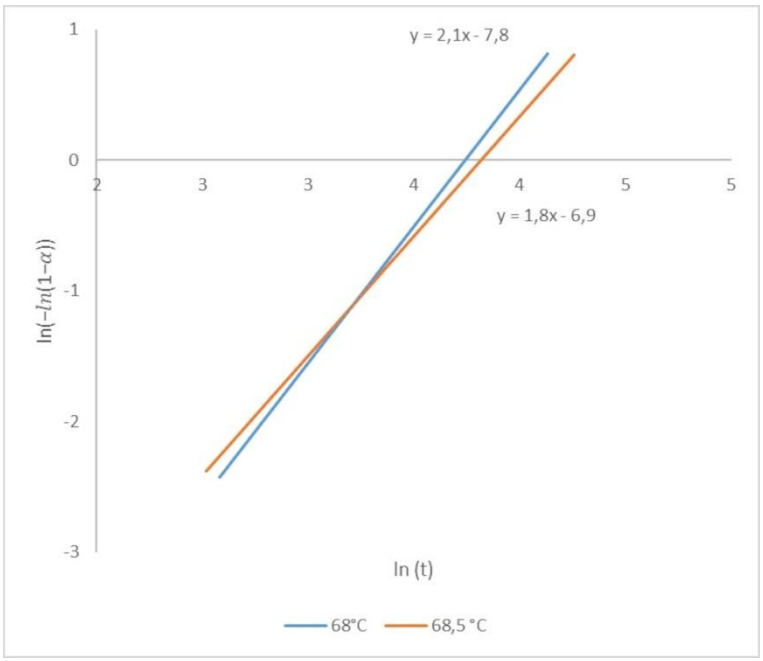

Figure 13: ln $(-ln\ (1-\alpha_1))$ versus ln (t) for the first transformation for two temperatures.

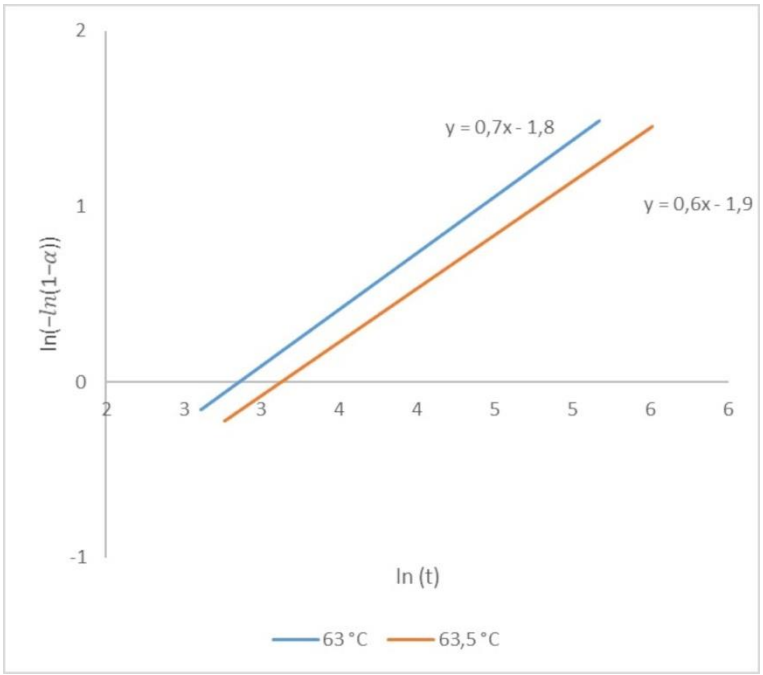

Figure 14 : ln $(-ln\ (1-\alpha_2))$ versus ln (t) for the second transformation for two temperatures.

Table 1 : Avrami coefficients and exponents KAvrami and n, calculated from the DSC isothermal tests

	Isothermal temperature (°C)	K_{Avrami} (s^{-n})	n (-)	Average value of n
First Transformation	69.3	$1.31\ 10^{-3}$	1.4	1.8
	69	$1.84\ 10^{-3}$	1.5	
	68.8	$1.92\ 10^{-3}$	1.6	
	68.5	$1.21\ 10^{-3}$	1.7	
	68.3	$9.31\ 10^{-4}$	1.8	
	68	$4.14\ 10^{-4}$	2.1	
	67.8	$2.90\ 10^{-4}$	2.2	
	67.5	$2.41\ 10^{-4}$	2.3	
Second transformation	63.5	0.24	0.7	0.7
	63.3	0.16	0.7	
	63	0.15	0.6	
	62.5	0.14	0.7	

The evolution of the K_{Avrami} coefficient in function of the temperature for the first transformation is plotted in *Figure 15*, and in *Figure 16* for the second transformation. This process could be operated only for a restricted temperature ranges that do not cover to full phase change temperatures: 68°C to 63.5°C for the first transformation and 63.5 to 62.5°C for the second. Indeed, outside these temperature ranges, the crystallization peaks appear during the temperature ramp.

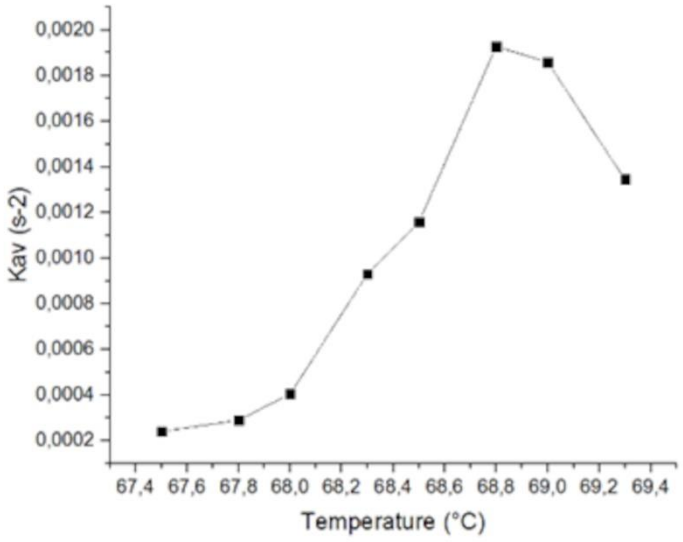

Figure 15 : K_{Avrami} coefficients versus the temperature for the first transformation

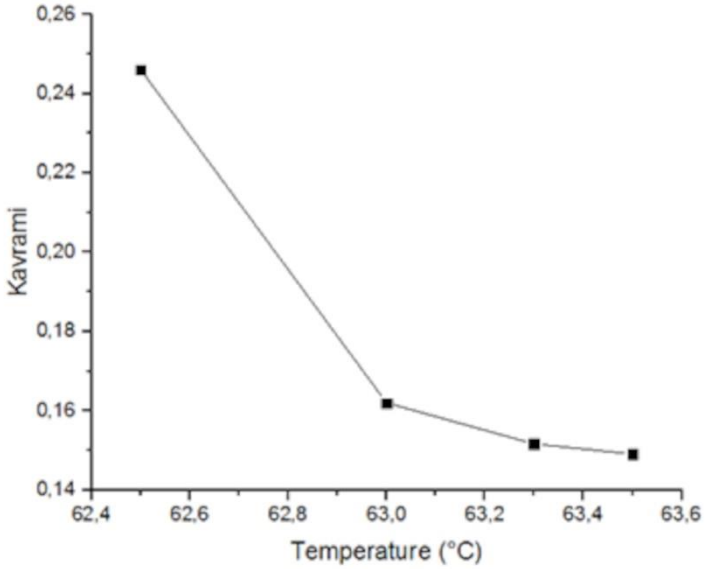

Figure 16: K_{Avrami} coefficients versus the temperature for the second transformation

The K_{Avrami} coefficients plots for the first transformation has the shape of a bell as described by the theory [21] [22] [23] with a maximum located at 68.8°C. As expected, for the second transformation, the K_{Avrami} coefficients plot is limited to the end of the bell due to the restriction of the method and the overlapping of the DSC curves. Therefore, for the second transformation, the temperature of the K_{Avrami} maximum is experimentally undetermined. This method which led to uncompleted description of the crystallization kinetic, requires to be completed by another technique described in section 3.2.

2.2.2. Crystallisation visualisation

The value of 2 for the Avrami exponent for the first peak, means that the crystals are in shape of rods with sporadic germination, or in discs with instantaneous germination. Sporadic germination means that the germs are not activated at the same time while instantaneous germination indicates that all the germs are activated from the crystallization beginning. For the second transformation, the value of 1 for the Avrami exponent means that the crystal growing is in rods shape with instantaneous germination.

To identify the entities shape and the germination type, a visualization experiment was carried out. A thermal cycle has been imposed to a RT70HC paraffin sample enclosed between two plastic plates and observed using an Olympus BX61 microscope. The thermal cycles were identical as these applied using the DSC device. During the crystallization process, several pictures were recorded and analysed.

Figure 17 shows a picture of the PCM at 68 °C, at the beginning of the crystallization for the first transformation, and in Figure 18, after 30 minutes at this same temperature.

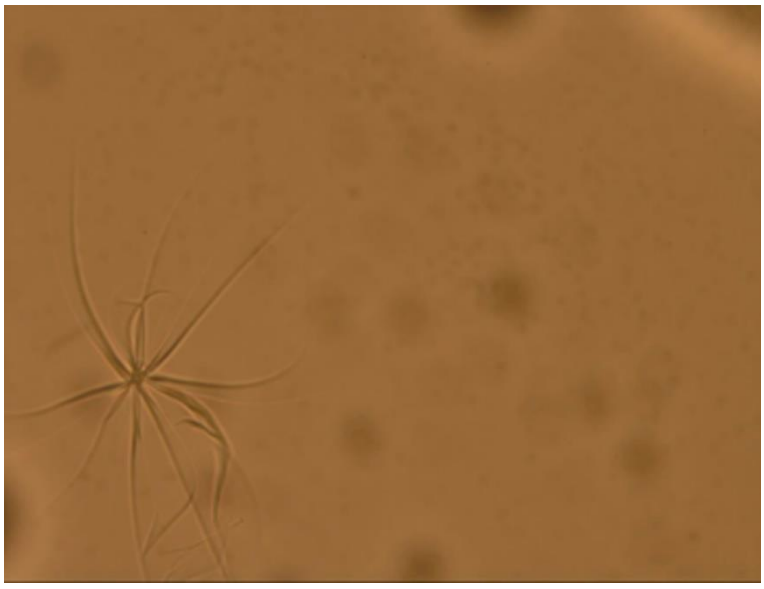

Figure 17: Picture of the PCM crystal structure at 68°C, at the beginning of the first transformation (picture width = 26mm).

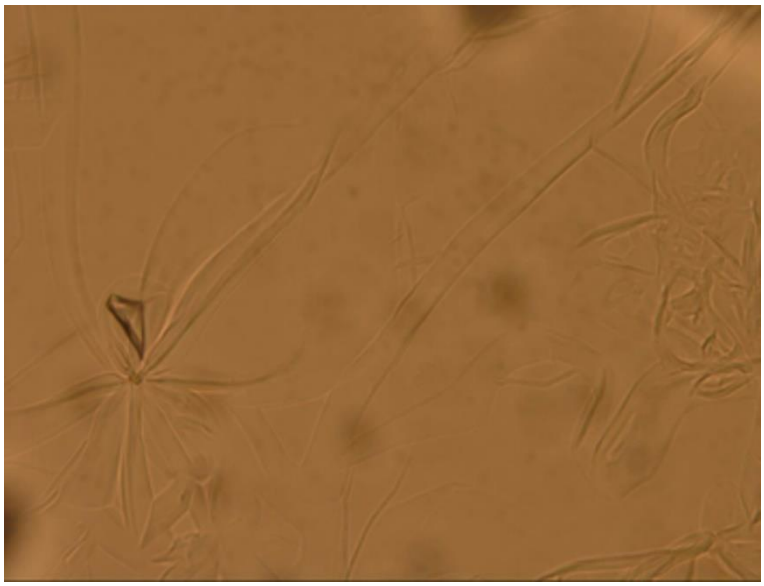

Figure 18: Picture of PCM crystal structure at 68°C, 30 minutes after the beginning of the first transformation (picture width =26mm).

The two figures show that the entities shape is rods with a sporadic germination. Indeed, we observe a heterogeneous nucleation that appears on impurities. These results confirm that the Avrami coefficient is equal to 2.

Figure 19 shows a picture of the PCM at 62 °C at the beginning of the second transformation and 30 minutes after the reaction started in Figure 20.

.

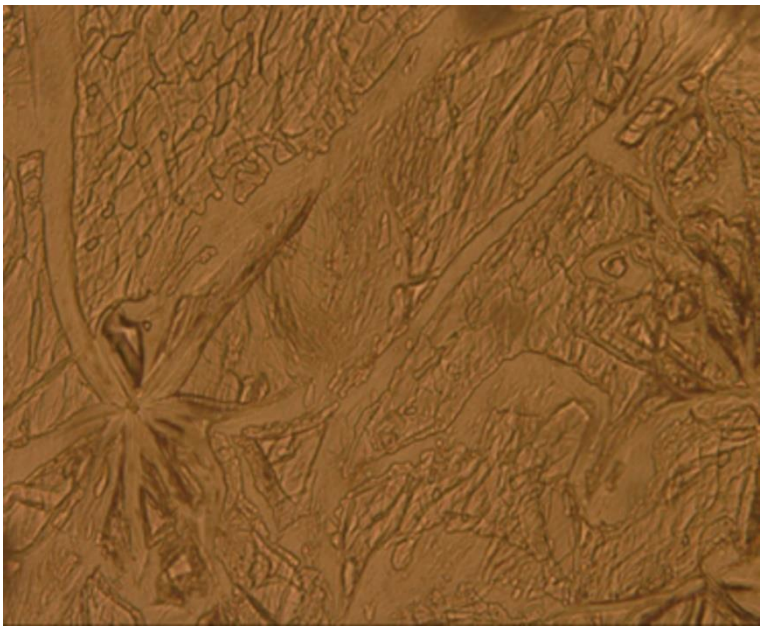

Figure 19: Picture PCM crystal structure at 62°C, at the beginning of the second transformation (picture width = 26mm)

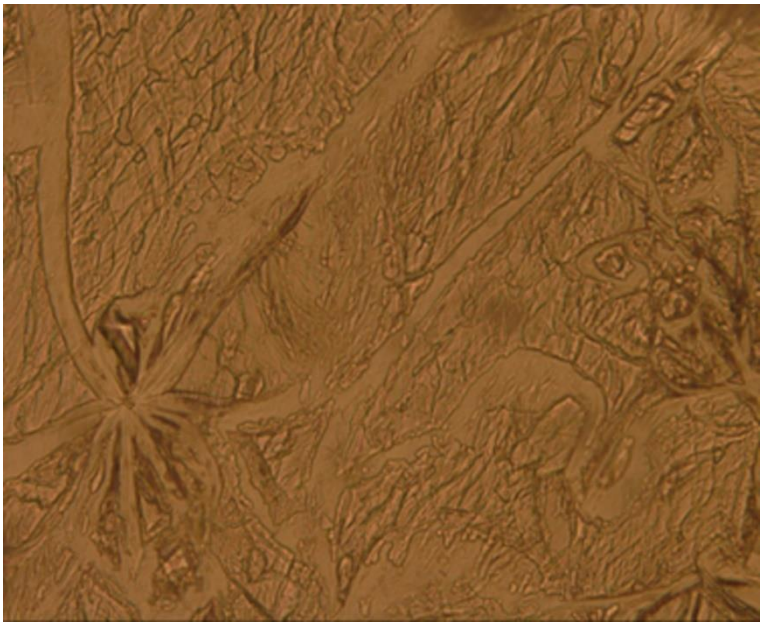

Figure 20: Picture of PCM crystal structure at 62°C, 30 minutes after the beginning of the second transformation (picture width = 26mm)

For the second transformation, the two figures show that the type of growing is also in rods shape. Nevertheless, in this case, the germination type is instantaneous as no change appears between the two pictures. This result confirms the value of the Avrami exponent *n* can be taken

to 1. From these visualization experiments, we can conclude that two different populations are present in the RT70HC paraffin with a different starting crystallization temperature.

2.2.3. Nakamura model non-isothermal kinetic model

The Avrami model, described in the previous section, is valid only in isothermal condition. This model can be extended to a non-isothermal case with a non-constant cooling rate. This formulation, called Nakamura model [25,26], is usually preferred because it is, in addition to be easier to implement in the numerical model, more adapted for all the cooling configurations. The Nakamura model parameters could be theoretically determined using specific tests with different cooling rates. However, in this case, the separation of the two transformations is quasi impossible to obtain due to the kinetics and the temperature ranges of each transformation very close of the two crystallisations.

The Nakamura formulation is given by the following equation.

$$\frac{d\alpha}{dt} = n \times K_{Avrami}(T)^{\frac{1}{n}} \times (1-\alpha) \times \left[\ln\left(\frac{1}{1-\alpha}\right)\right]^{\frac{n-1}{n}} \qquad \text{Equation 4}$$

where the $K_{Nakamura}$ coefficients can be calculated from K_{Avrami} coefficients using Equation 5.

$$K_{Nakamura} = {K_{Avrami}}^{1/n} \qquad \text{Equation 5}$$

with *n*, the Avrami exponent.

Figure 21 and Figure 22 respectively show the evolution of $K_{Nakamura}$ in function of the temperature for the first and for the second transformation. These functions will be implemented later in the numerical model.

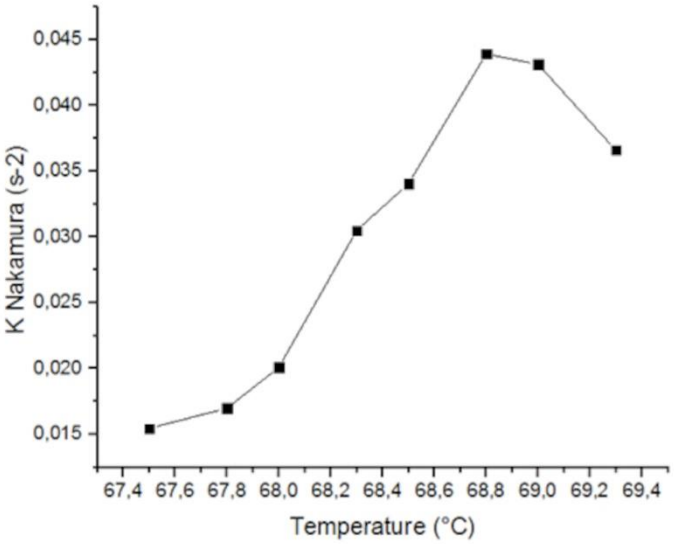

Figure 21: $K_{Nakamura}$ coefficients in function of the temperature for the first transformation

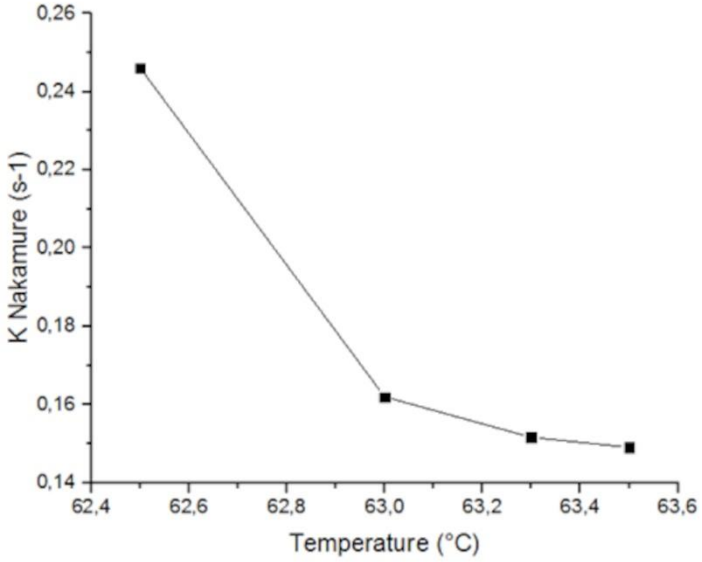

Figure 22: $K_{Nakamura}$ coefficients in function of the temperature for the second transformation

3. Validation of the model at micro and macro scales

3.1. Validation at micro-scale using DSC with RT70HC paraffin

The Nakamura model was validated using a DSC experiment where the heat flux measured from the DSC was compared to the heat flux calculated from crystallization kinetic model. The heat flux $\Phi(t)$ is modelized using the following equations where the crystallization is modelized using a source term gathering both transformations.

Domain without phase change:

$$\Phi(t) = m \,.\, C_p . \frac{dT}{dt} \qquad \text{Equation 6}$$

Domain with phase change:

$$\Phi(t) = m . C_p . \frac{dT}{dt} + m . \Delta H_T . (\omega_1 \frac{d\alpha_1}{dt} + \omega_2 \frac{d\alpha_2}{dt}) \qquad \text{Equation 7}$$

with:

$$\Delta H_T = \Delta H_1 + \Delta H_2 \qquad \text{Equation 8}$$

and

$$\omega_1 = \frac{\Delta H_1}{\Delta H_T} \qquad \text{Equation 9}$$

$$\omega_2 = \frac{\Delta H_2}{\Delta H_T} \qquad \text{Equation 10}$$

The solidified fractions $\alpha_1$and $\alpha_2$for the first and the second transformations are given using the differential form of Nakamura model:

$$\frac{d\alpha_1}{dt} = n_1 \times K_{Avrami}(T)^{\frac{1}{n_1}} \times (1 - \alpha_1) \times \left[\ln\left(\frac{1}{1-\alpha_1}\right)\right]^{\frac{n_1-1}{n_1}} \qquad \text{Equation 11}$$

$$\frac{d\alpha_2}{dt} = n_2 \times K_{Avrami}(T)^{\frac{1}{n_2}} \times (1 - \alpha_2) \times \left[\ln\left(\frac{1}{1-\alpha_2}\right)\right]^{\frac{n_2-1}{n_2}} \qquad \text{Equation 12}$$

with *m* the mass of the sample, C_p the specific heat, $\frac{dT}{dt}$ the cooling rate, ΔH_T the total enthalpy of transformation, ΔH_1 the enthalpy of the first transformation, ΔH_2 the enthalpy of the second transformation, ω_1 the enthalpy ratio of the first transformation to the total enthalpy, ω_2 the enthalpy ratio of the second transformation to the total enthalpy, α_1 and α_2 are respectively the solidified fraction of the first and the second transformations , and n_1 and n_2 are respectively the Avrami exponents of the first and the second transformations.

To complete the description of the $K_{Nakamura}$ evolution of the second peak in a wider temperature range that covers the full phase change, a polynomial extrapolation of the coefficients was carried out. The method is presented in section 3.2.

Three cooling rates were studied, 1 K.min^{-1} (*Figure 23*), 5 K.min^{-1} (*Figure 24*) and 10 K.min^{-1} (*Figure 25*).

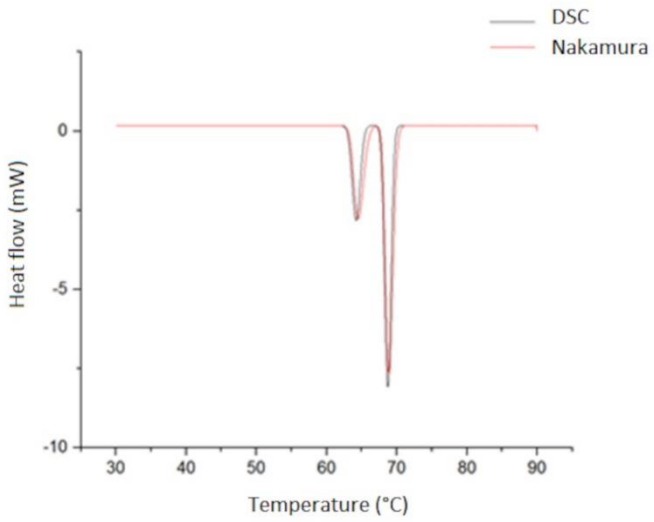

Figure 23: Heat flux versus the temperature obtained by DSC and calculated (1 $K.min^{-1}$)

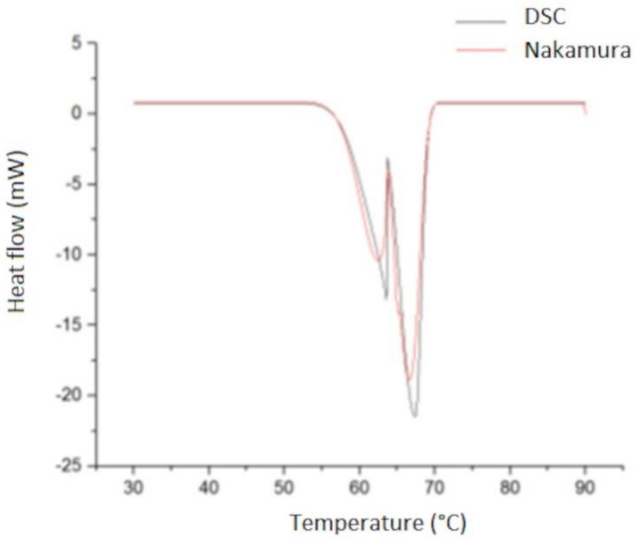

Figure 24: Heat flux versus the temperature obtained by DSC and calculated (5 $K.min^{-1}$)

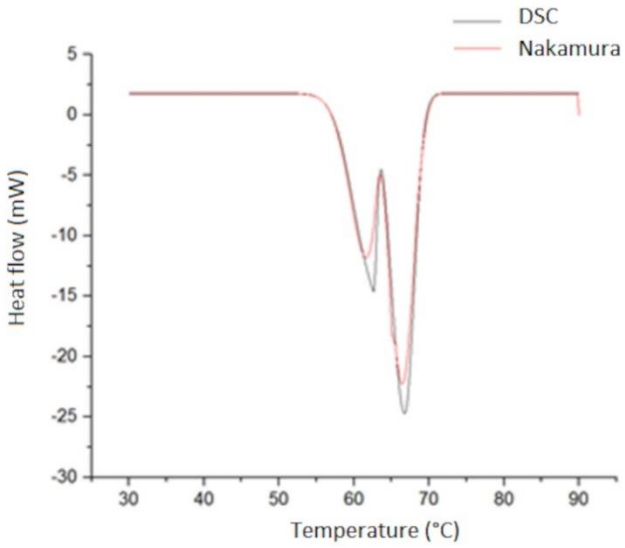

Figure 25: Heat flux versus the temperature obtained by DSC and calculated (10 K.min^{-1})

The experimental and calculated heat fluxes evolutions for the different cooling rates are very close. The two peaks are correctly represented, and the heat flux magnitudes are correctly modelized. To observe if there is a scale effect, the model of crystallization kinetics was validated at larger scale.

3.2. Validation at macroscale with an encapsulated CENG-RT70HC configuration

The validation of the model for the CENG-RT70HC was not performed using a DSC analysis. Indeed, the uncertainties of the mass fraction of CENG and paraffin for a small sample required for the DSC, few grams, are too high to obtain acceptable quantitative results. Therefore, a validation at macro-scale was performed with a packed bed heat exchanger configuration where the bed is composed of 600 encapsulated RT70HC-CENG composite cylinders (Figure 26). Each capsule is 18 mm diameter, 22 mm height, encapsulated with a 0.5 mm of aluminium shell (Figure *27*). The temperatures at the surface of the capsule, T_1, and in the centre of the CENG-MCP sample, T_2, were measured using 0.1 mm diameter type K thermocouples, with a ± 0.1K measurement uncertainty in the temperature range studied (Figure *28*).

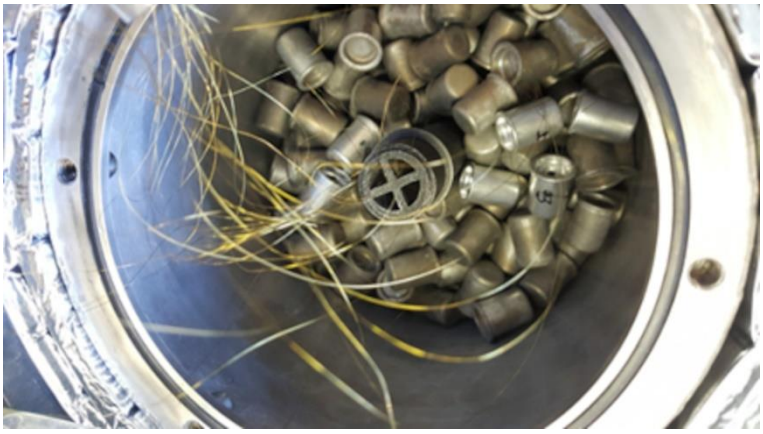

Figure 26 : Picture of the packed bed heat storage exchanger viewed from the top with a partial filling of aluminium capsules of CENG-RT70HC material

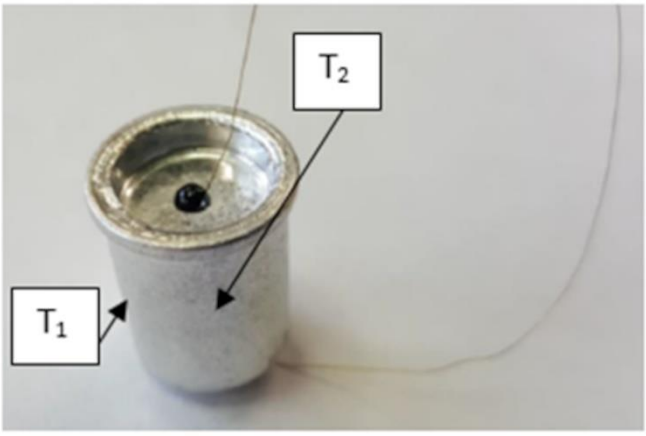

Figure 27 : Picture of CENG-RT70HC encapsulated in aluminium shell and equipped with thermocouples in the centre.

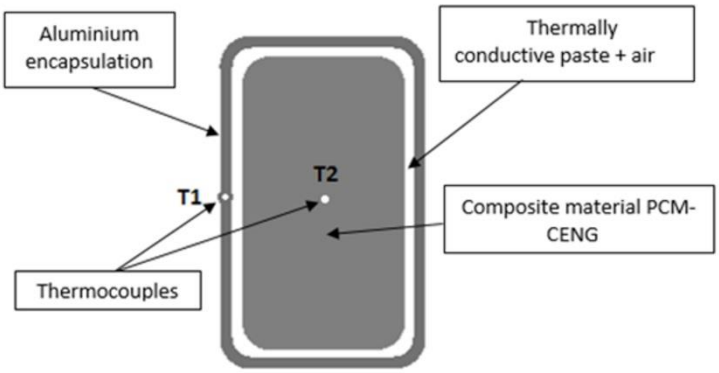

Figure 28 : Location of the thermocouple in the encapsulated PCM-CENG capsule

In the experimental test, the heat storage exchanger was cooled down from 88°C to 20°C. The temperatures of the capsule were recorded and compared to a numerical simulation in Comsol Multiphysics software, where the Nakamura model was implemented in the energy equation. The equations solved are the following:

$$\rho(T,\alpha).C_p(T,\alpha).\frac{\partial T}{\partial t} = div[k(T,\alpha).gradT] + \rho(T,\alpha).\Delta H_T\left(\omega_1\frac{d\alpha_1}{dt} + \omega_2\frac{d\alpha_2}{dt}\right) \quad \text{Equation 13}$$

With

$$\frac{d\alpha_1}{dt} = n_1 \times K_{Nakamura}(T) \times (1-\alpha_1) \times \left[\ln\left(\frac{1}{1-\alpha_1}\right)\right]^{\frac{n_1-1}{n_1}} \quad \text{Equation 14}$$

$$\frac{d\alpha_2}{dt} = n_2 \times K_{Nakamura}(T) \times (1-\alpha_2) \times \left[\ln\left(\frac{1}{1-\alpha_2}\right)\right]^{\frac{n_2-1}{n_2}} \quad \text{Equation 15}$$

where the density $\rho(T,\alpha)$, the specific heat $C_p(T,\alpha)$, and the thermal conductivity $k(T,\alpha)$ are calculated in solid and liquid phases using their values measured experimentally [38]. The properties values are display in table 2. During the transition phase, the values of these properties are calculated using the solid fraction α which weights the values in liquid and solid phases (Equation 17). For example, the density during phase change is given by Equation 16.

$$\rho = \alpha\, \rho_{solid} + (1-\alpha)\rho_{liquid} \quad \text{Equation 16}$$

where

$$\alpha = \omega_1\, \alpha_1 + \omega_2\, \alpha_2 \quad \text{Equation 17}$$

Table 2: CENG-RT70HC properties

Property	**Liquid**	**Solid**
ρ [kg.m^{-3}]	750	880
C_p [J.kg^{-1}.K^{-1}]	2 400	2 200
k in planar direction [W.m^{-1}.K^{-1}]	20.9	20.3
k in transversal direction [W.m^{-1}.K^{-1}]	6.4	6.2

The temperature at the centre of the capsule T_2 was calculated using a 2D axisymmetric geometry with the surface temperature T_1 as boundary condition taken from the experimental test. A thermal resistance between the aluminium and the composite material was estimated and implemented.

In a first step, the $K_{Nakamura}$ coefficients implemented in the model are given by the isothermal experiments in the range of temperature 69.4°C to 67.5°C for the first transformation and 63.5 to 62.5°C for the second transformation. Between 67.5°C and 63.5°C, zero is taken for the $K_{Nakamura}$ coefficients. This assumption leads to consider the solidified fraction constant.

The experimental and calculated temperatures are plotted in Figure 29. We can observe a plateau at 69°C, followed by a quasi-plateau starting at 63.5°C, due to the two exothermic transformations. In the solidification phase, the enthalpy of the first transformation is considered. However, the enthalpy of the second transformation is not simulated correctly due to the uncompleted $K_{Nakamura}$ coefficients description in this temperatures range.

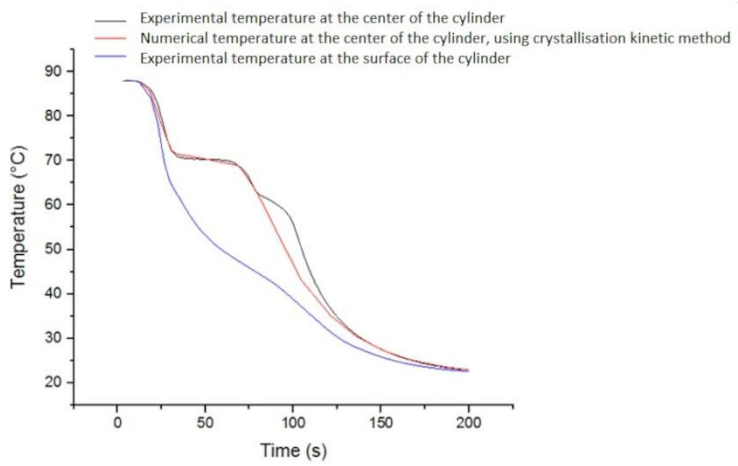

Figure 29: Time evolution of the temperature at the centre of the sample obtained experimentally and numerically during the cooling of the packed PCM bed.

To solve this problem, an extrapolation of the $K_{Nakamura}$ coefficients as a function of temperature with bell form was attempted by doing an analogy between the two transformations. For the first transformation, the maximum of $K_{Nakamura}$ coefficients was obtained at 68.8 °C (Figure 30). This temperature corresponds to the inflexion point of the temperature time evolution curve *i. e.* when the third derivative of the temperature versus time is zero.

This inflexion point was visualized through the evolution of the slope of the temperature in function of time (Figure *31*). The inflexion point for the second transformation is located at 57.8°C. In consequence, we decided to impose this temperature as the maximum temperature of crystallization kinetics, when the $K_{Nakamura}$ coefficients is maximum.

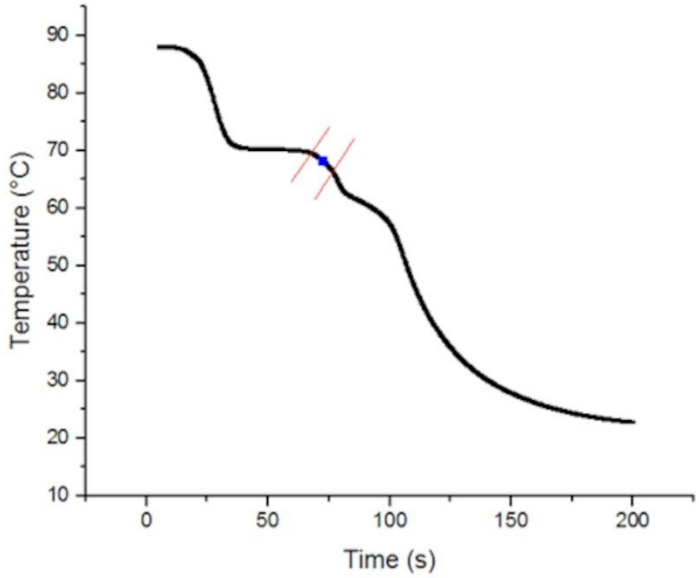

Figure 30: Time evolution of the temperature in the centre of the sample for a cooling test where the blue dot is the temperature when the $K_{Nakamura}$ coefficients is maximum.

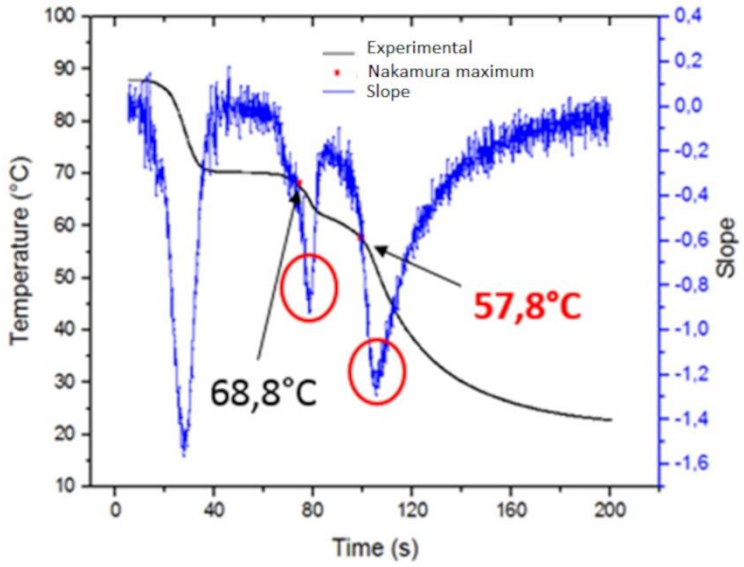

Figure 31: Temperature and temperature variation versus time

The extrapolation of the $K_{Nakamura}$ coefficient in the full range temperature transformation was carried out based on the following assumptions. We imposed that the coefficient $K_{Nakamura}$ is zero at its melting temperature, 70°C. Indeed, the crystallisation has not started at this stage. Also, the coefficient $K_{Nakamura}$ is zero when the crystallization is completed. At this temperature, 30°C, there is a weak mobility of the macromolecular chains and the crystallization rate is zero. With these assumptions, we can complete the $K_{Nakamura}$ description versus the temperature using interpolation and extrapolation (*Figure 32*).

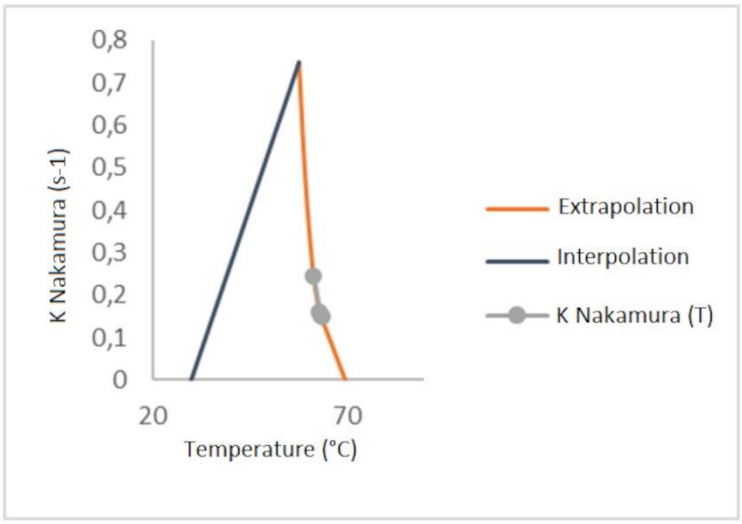

Figure 32: $K_{Nakamura}$ coefficients versus temperature for the second transformation

These values have been implemented in the numerical model in Comsol Multiphysics, for a second resolution. The temperature time evolution is now well described including during the second transformation (*Figure 33*). The model defined for the paraffin is then valid for the paraffin impregnated in CENG. The CENG does not act as a nucleating agent or change significantly the crystallisation kinetic such as observed with talc in PLA [39] or graphene in

lauric acid [40]. This conclusion could be expected as the nucleation process is heterogeneous with this paraffin.

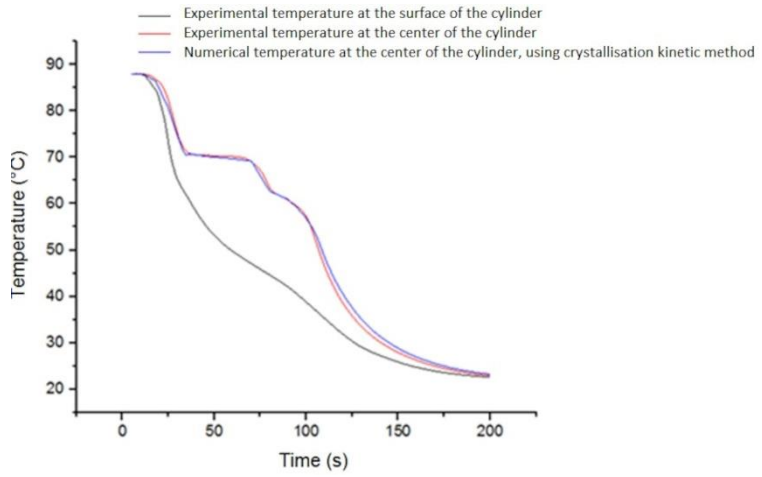

Figure 33: Temperatures at the centre and at the surface of the ball obtained experimentally and numerically during the cooling test.

3.3. Validation at macroscale in a CENG-RT70HC plate configuration

An experimental device has been developed with the aim to heat and cool a plate from one side (Figure 34). The material used is similar of those used in the encapsulated cylinders *i. e.* a CENG-RT70HC composite. The 143 × 143 × 20mm composite plate is heated or cooled on its side with a hollow copper part where a heat transfer fluid can circulate (Figure 35). The heat diffuses in the plane direction of the composite material. The plate is surrounded by two PTFE plates to limit thermal losses, and two exchangers to impose a temperature during the tests.

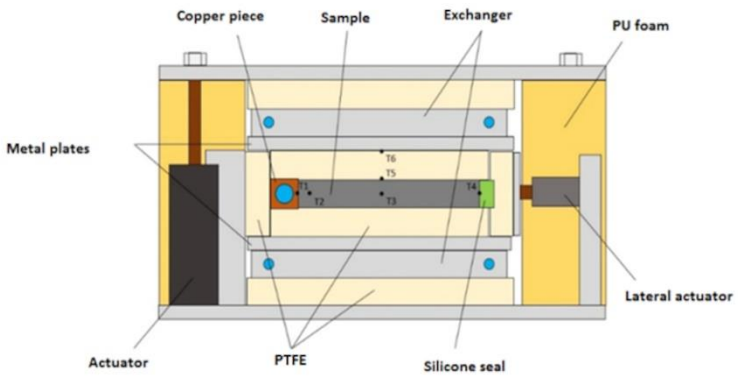

Figure 34: Experimental device for heating and cooling a plate on its side.

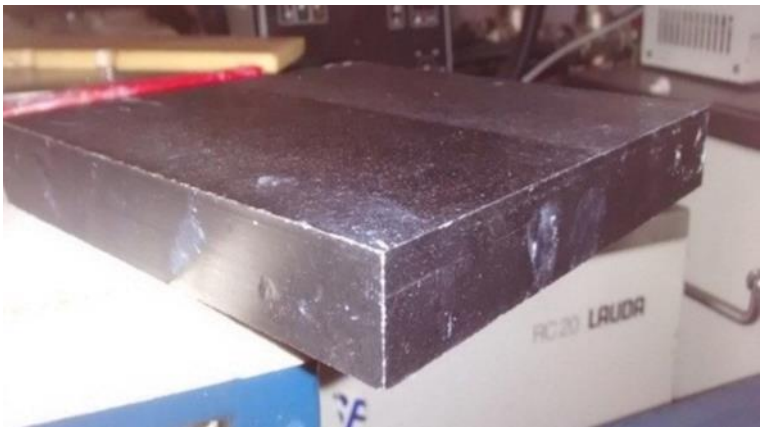

Figure 35: CENG-PCM composite material picture.

Several micro-thermocouples are positioned in the composite plate (T_1, T_2 and T_3), at the interface of the composite plate and the PTFE panel (T_4 and T_5), and at the interface of the PTFE panel and the heat exchanger (T_6) as shown in Figure 36.

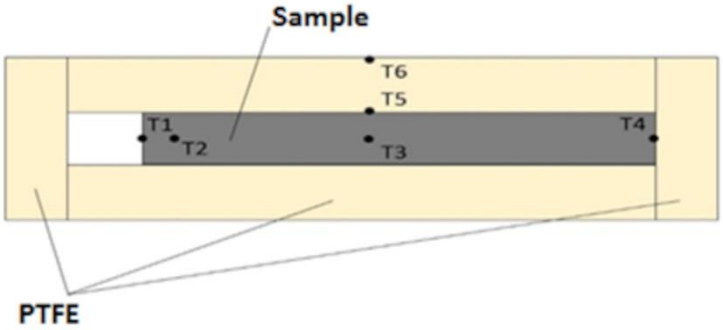

Figure 36 : Thermocouples location in the experimental device

The first thermocouple (T_1) is positioned between the sample interface and the copper part, the second is 10 mm away from the copper part (T_2). The third thermocouple located 71.5mm for the copper part (T_3) is in the middle of the sample.

The experimental test was simulated in Comsol Multiphysics by imposing the temperatures at the boundary conditions T_1 and T_6, and convective heat exchange coefficients calculated by inverse method (*Figure 37*). And addition, the contact thermal resistance between the sample and the copper part, the PTFE and the heat exchangers are calculated by inverse method [38]. These boundary conditions were identified in solid and liquid phase. The final converged values are given in Table 3.

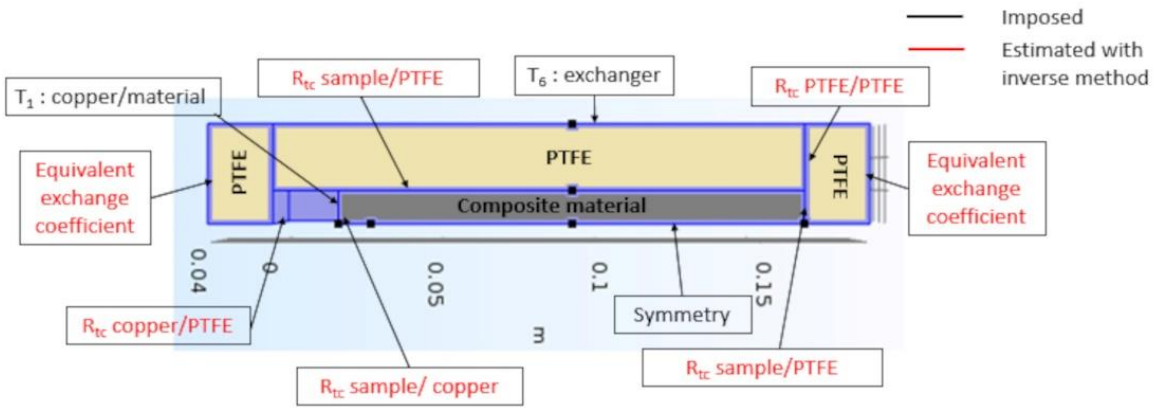

Figure 37: Boundary conditions imposed in the numerical model

The thermal properties of the material were measured by various conventional techniques, guarded hot plate, DSC, dilatometer, in liquid and in solid phases.

Table 3: Parameters obtained by inverse method in solid and liquid phases

	Solid phase	**Liquid phase**
Planar thermal conductivity	20.3 $W.m^{-1}.K^{-1}$	20.9 $W.m^{-1}.K^{-1}$
Thermal resistance between sample and copper part	1.7 10^{-4} $m^2.K.W^{-1}$	9.4 10^{-5} $m^2.K.W^{-1}$
Thermal resistance between sample and PTFE	1.6 10^{-2} $m^2.K.W^{-1}$	2.7 10^{-5} $m^2.K.W^{-1}$
Thermal resistance between copper and PTFE	1.5 10^{-3} $m^2.K.W^{-1}$	1.5 10^{-3} $m^2.K.W^{-1}$
Thermal resistance between two PTFE plates	2.5 10^{-6} $m^2.K.W^{-1}$	2.5 10^{-6} $m^2.K.W^{-1}$
Convective heat transfer coefficient	1 $W.m^{-2}.K^{-1}$	1 $W.m^{-2}.K^{-1}$

The experimental test consisted in cooling the composite plate initially at 80°C from its side with a copper part at 55°C. The temperatures within the composite plate T_2 and T_3 are measured during the cooling and compared with the numerical simulation. The results shown in Figure 38, demonstrated a very satisfactory agreement, with a 0.03 K mean square error between the two temperatures.

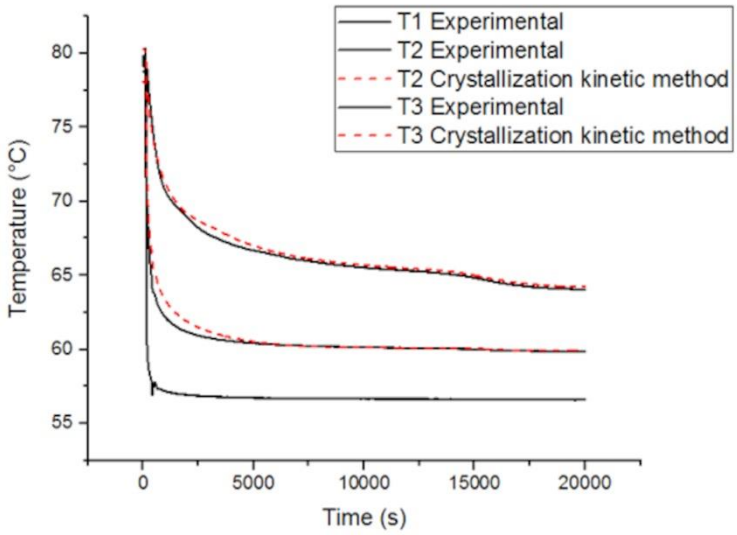

Figure 38: T_2 and T_3 evolution obtained experimentally and numerically during the cooling of the CENG-RT70HC composite plate.

4. Conclusion

The method for modelling the kinetic of the crystallisation of a CENG-RT70HC composite has been presented. We found that the CENG does not act as a nucleating agent and does not seem to affect the kinetic properties of the RT70HT Phase Change Material. Therefore, the kinetic study can be performed on a PCM sample, and the be applied to a CENG-PCM composite. In addition, as expected, we did not observe a scale effect. The kinetic crystallisation behaviour remains the same whatever the PCM matrix shape, size, and cooling rate.

For PCM showing a two steps crystallisation process, like the RT70HC, the description of the kinetic is uneasy using only the DSC analysis because of the two overlapping exothermic reactions occurring during the cooling. Therefore, this analysis has to be completed with an additional experiment where the encapsulated CENG-PCM sample was cooled with a convective constant temperature. This experiment, that can be considered as a macro-DSC, allowed to perform an analogy between the two transformations and the guessed a maximum for the Nakamura coefficients. To complete the description of the kinetic on the full phase change temperature range, an interpolation and an extrapolation were achieved.

The kinetic crystallisation model has been implemented in the energy equation as a source term. The Nakamura formulation was used to respond to the general case of an isothermal cooling. This phase change model that has been successfully validated on two configurations, is very suitable for taking into account the phase change considering the temperature history of the PCM in regard to enthalpic formulation where the analytical models of the phase change, including partial solidification, is challenging [19].

Acknowledgements
The authors want to acknowledge Nicolas LEFEVRE, Arnaud ARRIVE and Julien AUBRIL for their technical support.

Funding
This work was supported by the ERDF Pays de la Loire CIPITAP programme 2014-2020, by the French Environment and Energy Management Agency ADEME and the Pays de la Loire Region.

References

[1] J.M.P.Q. Delgado, J.C. Martinho, A. Vaz Sá, A.S. Guimarães, V. Abrantes, Thermal Energy Storage with Phase Change Materials, A Literature Review of Applications for Buildings Materials, 2019. https://doi.org/10.1007/978-3-319-97499-6.

[2] F. Kuznik, D. David, K. Johannes, J.J. Roux, A review on phase change materials integrated in building walls, Renew. Sustain. Energy Rev. 15 (2011) 379–391. https://doi.org/10.1016/j.rser.2010.08.019.

[3] L.F. Cabeza, a. Castell, C. Barreneche, a. De Gracia, a. I. Fernández, Materials used as PCM in thermal energy storage in buildings: A review, Renew. Sustain. Energy Rev. 15 (2011) 1675–1695. https://doi.org/10.1016/j.rser.2010.11.018.

[4] S. Landini, J. Leworthy, T.S.O. Donovan, A Review of Phase Change Materials for the Thermal Management and Isothermalisation of Lithium-Ion Cells, J. Energy Storage. 25 (2019) 100887. https://doi.org/10.1016/j.est.2019.100887.

[5] J. Jaguemont, N. Omar, P. Van Den Bossche, J. Mierlo, Phase-change materials (PCM) for automotive applications : A review, Appl. Therm. Eng. 132 (2018) 308–320. https://doi.org/10.1016/j.applthermaleng.2017.12.097.

[6] H. Fathabadi, High thermal performance lithium-ion battery pack including hybrid active-passive thermal management system for using in hybrid/electric vehicles, Energy. 70 (2014) 529–538. https://doi.org/10.1016/j.energy.2014.04.046.

[7] M. Gumus, Reducing cold-start emission from internal combustion engines by means of thermal energy storage system, Appl. Therm. Eng. 29 (2009) 652–660. https://doi.org/10.1016/j.applthermaleng.2008.03.044.

[8] Q. Ren, P. Guo, J. Zhu, International Journal of Heat and Mass Transfer Thermal management of electronic devices using pin-fin based cascade microencapsulated PCM / expanded graphite composite, 149 (2020) 1–16. https://doi.org/10.1016/j.ijheatmasstransfer.2019.119199.

[9] H. Muhammad, A. Arshad, M. Jabbal, P.G. Verdin, International Journal of Heat and Mass Transfer Thermal management of electronics devices with PCMs filled pin-fin heat sinks : A comparison, Int. J. Heat Mass Transf. 117 (2018) 1199–1204. https://doi.org/10.1016/j.ijheatmasstransfer.2017.10.065.

[10] S. Kumar, M.K. Das, P. Rath, Application of TCE-PCM based heat sinks for cooling of electronic components : A review, Elsevier, 2016. https://doi.org/10.1016/j.rser.2015.12.238.

[11] M.E. Zayed, J. Zhao, A.H. Elsheikh, F.A. Hammad, L. Ma, Y. Du, A.E. Kabeel, S.M. Shalaby, Solar Energy Materials and Solar Cells Applications of cascaded phase

change materials in solar water collector storage tanks : A review, Sol. Energy Mater. Sol. Cells. 199 (2019) 24–49. https://doi.org/10.1016/j.solmat.2019.04.018.

[12] B. Stutz, N. Le Pierres, F. Kuznik, K. Johannes, E. Palomo Del Barrio, J.-P. Bédécarrats, S. Gibout, P. Marty, L. Zalewski, J. Soto, N. Mazet, R. Olives, J.-J. Bezian, D.P. Minh, Storage of thermal solar energy, Comptes Rendus Phys. 18 (2017). https://doi.org/10.1016/j.crhy.2017.09.008.

[13] B. Xu, P. Li, C. Chan, Application of phase change materials for thermal energy storage in concentrated solar thermal power plants : A review to recent developments, Appl. Energy. 160 (2015) 286–307. https://doi.org/10.1016/j.apenergy.2015.09.016.

[14] H. Mehling, S. Hippeli, S. Hiebler, L.F. Cabeza, PCM-module to improve hot water heat stores with stratification, Renew. Energy. 28 (2003) 699–711. https://doi.org/10.1016/S0960-1481(02)00108-8.

[15] L.T. Wong, K.W. Mui, Y. Guan, Shower water heat recovery in high-rise residential buildings of Hong Kong, Appl. Energy. 87 (2010) 703–709. https://doi.org/10.1016/j.apenergy.2009.08.008.

[16] P. Royo, L. Acevedo, V.J. Ferreira, T. García-Armingol, A.M. López-Sabirón, G. Ferreira, High-temperature PCM-based thermal energy storage for industrial furnaces installed in energy-intensive industries, Energy. 173 (2019) 1030–1040. https://doi.org/10.1016/j.energy.2019.02.118.

[17] L. Miró, J. Gasia, L.F. Cabeza, Thermal energy storage (TES) for industrial waste heat (IWH) recovery: A review, Appl. Energy. 179 (2016) 284–301. https://doi.org/10.1016/j.apenergy.2016.06.147.

[18] K. Merlin, J. Soto, D. Delaunay, L. Traonvouez, Industrial waste heat recovery using an enhanced conductivity latent heat thermal energy storage, Appl. Energy. 183 (2016) 491–503. https://doi.org/10.1016/j.apenergy.2016.09.007.

[19] M. Thonon, G. Fraisse, L. Zalewski, M. Pailha, Analytical modelling of PCM supercooling including recalescence for complete and partial heating/cooling cycles, Appl. Therm. Eng. 190 (2021) 116751. https://doi.org/10.1016/j.applthermaleng.2021.116751.

[20] J.P. Dumas, Models for the heat transfers during the transformations Crystallizations of the undercooled droplets, 37 (1994).

[21] M. Avrami, Kinetics of phase change. I : general theory, J. Chem. Phys. 7 (1939) 1103–1112.

[22] M. Avrami, Kinetics of phase change II : transformation-time relations for random distribution of nuclei, J. Chem. Phys. 8 (1940) 224.

[23] M. Avrami, Kinetics of phase change. III : Granulation, phase change, and microstructure., J. Chem. Phys. 9 (1941) 177–184.

[24] T. Ozawa, Kinetics of non-isothermal, Polymer (Guildf). 12 (1971) 150–158.

[25] T. Nakamura, K. Wantanabe, K., Katayama, K., and Amano, Some aspects of nonisothermal crystallization of polymers I : relationship between crystallization temperature, crystallinity, and cooling conditions, J. Appl. Polym. Sci. 16 (1972) 1077–1091.

[26] K. Nakamura, K. Katayama, T. Amano, Some Aspects of Nonisothermal Crystallization of Polymers . 11 . Consideration of the Isokinetic Condition, 17 (1973) 1031–1041.

[27] T. Choupin, Mechanical performances of PEKK thermoplastic composites linked to their processing parameters, ’École Nationale Supérieure d’Arts et Métiers de ParisTech, 2017.

[28] B.A. K.H. Gardner, B.S. Hsiao, R.R. Matheson, Wood, Structure, crystallization and morphology of poly (aryl ether ketone ketone), Polym. 33. (1992) 2483–2495. https://doi.org/doi:10.1016/0032-3861(92)91128-O.

[29] S.Z.D.C. B.S. Hsiao, K.H. Gardner, Crystallization of poly(aryl ether ketone ketone) copolymers containing terephthalate/isophthalate moieties, J. Polym. Sci. Part B Polym. Phys. 32 2585–2594. Doi10.1002/Polb.1994.090321604. (n.d.).

[30] R. Tamme, T. Bauer, J. Buschle, D. Laing, W. Steinmann, Latent heat storage above 120°C for applications in the industrial process heat sector and solar power generation, Int. J. Energy Res. 32 (2008) 264–271. https://doi.org/10.1002/er.

[31] Z. Tao, H. Wang, J. Liu, W. Zhao, Z. Liu, Q. Guo, Dual-level packaged phase change materials – thermal conductivity and mechanical properties, Sol. Energy Mater. Sol. Cells. 169 (2017) 222–225. https://doi.org/10.1016/j.solmat.2017.05.030.

[32] Z. Ling, J. Chen, T. Xu, X. Fang, X. Gao, Z. Zhang, Thermal conductivity of an organic phase change material/expanded graphite composite across the phase change temperature range and a novel thermal conductivity model, Energy Convers. Manag. 102 (2015) 202–208. https://doi.org/10.1016/j.enconman.2014.11.040.

[33] K. Merlin, D. Delaunay, J. Soto, L. Traonvouez, Heat transfer enhancement in latent heat thermal storage systems: Comparative study of different solutions and thermal contact investigation between the exchanger and the PCM, Appl. Energy. 166 (2016) 107–116. https://doi.org/10.1016/j.apenergy.2016.01.012.

[34] X. Py, R. Olives, S. Mauran, Paraffin/porous-graphite-matrix composite as a high and constant power thermal storage material, Int. J. Heat Mass Transf. 44 (2001) 2727–2737.

[35] M. Karthik, A. Faik, B.D. Aguanno, Preparation of erythritol – graphite foam phase change composite with enhanced thermal conductivity for thermal energy storage applications, Carbon N. Y. 94 (2015) 266–276. https://doi.org/10.1016/j.carbon.2015.06.075.

[36] T. Nomura, N. Okinaka, T. Akiyama, Impregnation of porous material with phase change material for thermal energy storage, Mater. Chem. Phys. 115 (2009) 846–850. https://doi.org/10.1016/j.matchemphys.2009.02.045.

[37] J. Soto; M. Jadal; N. DE Guyenro; D. Delaunay, Thermal cycling aging of encapsulated Phase Change Material – Compressed Expanded Natural Graphite composite, Therm. Sci. Eng. Prog. (2020) 1–23.

[38] M. JADAL;, Caractérisation thermique d’un échangeur-stockeur composé d’un matériau à changement de phase dans une structure conductrice, Thèse de doctorat, Université de Nantes, 2020.

[39] H. Li, M.A. Huneault, Effect of nucleation and plasticization on the crystallization of

poly (lactic acid), 48 (2007). https://doi.org/10.1016/j.polymer.2007.09.020.

[40] K. Liang, L. Shi, J. Zhang, J. Cheng, X. Wang, Thermochimica Acta Fabrication of shape-stable composite phase change materials based on lauric acid and graphene / graphene oxide complex aerogels for enhancement of thermal energy storage and electrical conduction, Thermochim. Acta. 664 (2018) 1–15. https://doi.org/10.1016/j.tca.2018.04.002.

Declaration of interests

☒The authors declare that they have no known competing financial interests or personal relationships that could have appeared to influence the work reported in this paper.

☐The authors declare the following financial interests/personal relationships which may be considered as potential competing interests: